RSC Advances

PAPER

View Article Online
View Journal | View Issue

Cite this: *RSC Adv.*, 2026, **16**, 3244

High-performance polyimide coatings for mild steel: the impact of benzophenone, biphenyl, and bisphenol-a core structures

Sukanta Badaik,†[ab] Suryakanta Nayak,*[b] Balram Ambade[a] and Tapan Kumar Rout*[b]

Engineered polyimide coatings are widely recognized for their high thermal stability, chemical resistance, mechanical strength, and electrical insulation. In this work, three polyamic acid (PAA) systems (PAA-1, PAA-2, and PAA-3) were synthesized using two diamines and varying dianhydrides [benzophenone-3,3′,4,4′-tetracarboxylic dianhydride (BTDA), 4,4′-Biphthalic Anhydride (BPDA) or 4,4′-bisphenol A diphthalic anhydride (BPADA)] to investigate the influence of benzophenone, biphenyl, and bisphenol-A cores on polyimide coating performance. The polyamic acid (PAA) solutions were prepared under a nitrogen atmosphere and subsequently imidized at 250 °C to obtain polyimide coatings (PI-1, PI-2, and PI-3) on mild steel substrates. This study provides insights into how structural variations in the polyimide backbone affect adhesion, thermal stability, and anticorrosion behaviour. Solid-state ^{13}C NMR, XPS, FTIR, and XRD confirmed structural integrity, imidization, and molecular packing, while SEM and CLSM revealed uniform surface morphology. PI-3 exhibited superior adhesion (3.03 MPa) due to Fe–O–C bond formation and demonstrated excellent corrosion resistance in salt spray testing (ASTM B117), with <5% red rust after 168 h. PI-2 (biphenyl core) showed the highest thermal stability and storage modulus (1915 MPa), whereas PI-3 (bisphenol-A core) achieved the highest loss modulus (297.46 MPa), tan δ (0.177), and crosslinking density (0.343 mol m^{-3}). Enhanced damping capability and chain mobility of PI-3 contribute to crack resistance and long-term anticorrosion performance, highlighting its potential for advanced protective applications.

Received 7th August 2025
Accepted 4th January 2026

DOI: 10.1039/d5ra05765e

rsc.li/rsc-advances

1. Introduction

Mild steel, often called carbon steel, is a versatile material which is manufactured using various methods, such as cold-rolled, hot-rolled, or galvanized processes, depending on the desired finish.[1] Despite its versatility, mild steel is prone to corrosion even with minimal exposure to environmental elements. To combat this susceptibility, protective coatings such as passivation coatings and polymeric coatings are generally used on mild steel surfaces, helping to minimize the effects of corrosion and extend the material's lifespan.[2,3] Polyimides are a class of high-performance polymers identified for their excellent thermal resistance, mechanical, and chemical resistance properties. Polyimide coatings offer a protective barrier against environmental factors, including moisture, chemicals, and temperature fluctuations, thus preventing the onset of corrosion.[4–6] In 1965, DuPont produced the first commercial PI film using a two-step process. In the first step, the polyamic acid (PAA) was synthesized from two types of monomers (dianhydride and diamine), followed by an exothermic polycondensation reaction using a dipolar solvent, such as *N*-methyl-2-pyrrolidone (NMP), *N*,*N*-dimethylformamide (DMF), or *N*,*N*-dimethylacetamide (DMAc). The second step is the thermal imidization reaction after removing the solvent from the PAA.[7] The mentioned polyimide is well known for its good mechanical and thermal stability.[8] Despite these properties, polyimide coatings play a crucial role in enhancing the corrosion resistance of mild steel by physically obstructing the diffusion of corroding species, *e.g.* H^+ and O_2.[9] However, the advancement in anti-corrosion coatings using 4,4′-bisphenol A diphthalic anhydride (BPADA), benzophenone-3,3′,4,4′-tetracarboxylic dianhydride (BTDA), and 4,4′-Biphthalic Anhydride (BPDA) on steel has been minimally explored. Polyimides or copolyimides prepared using BTDA have good thermal stability, flexibility, and robustness.[10–12] BPDA-based polyimides are transparent, thermal resistant, and crystalline in nature.[13–15] Similarly, BPADA-based polyetherimides have good thermal, chemical, and electrochemical properties.[16–20]

[a]*Department of Chemistry, National Institute of Technology Jamshedpur, 831014, India*

[b]*R&D, Surface Engineering Research Group, Tata Steel Limited, Jamshedpur 831001, India. E-mail: tapankumarrout@tatasteel.com; suryakanta.nayak@tatasteel.com*

† Joint PhD scholar of the Department of Chemistry, National Institute of Technology, Jamshedpur and R&D, Surface Engineering Research Group, Tata Steel Limited.

Table 1 Different coating formulations by varying the second dianhydride (BPDA/BTDA/BPADA)[a]

Coating solution	First diamine (ODA)	Second diamine (HMDA)	First dianhydride (PMDA)	Second dianhydride (BPDA/BTDA/BPADA)
PAA-1	0.5	0.5	0.5	0.5
PAA-2	0.5	0.5	0.5	0.5
PAA-3	0.5	0.5	0.5	0.5

[a] The concentration of all monomers is given as per 0.5 equivalent.

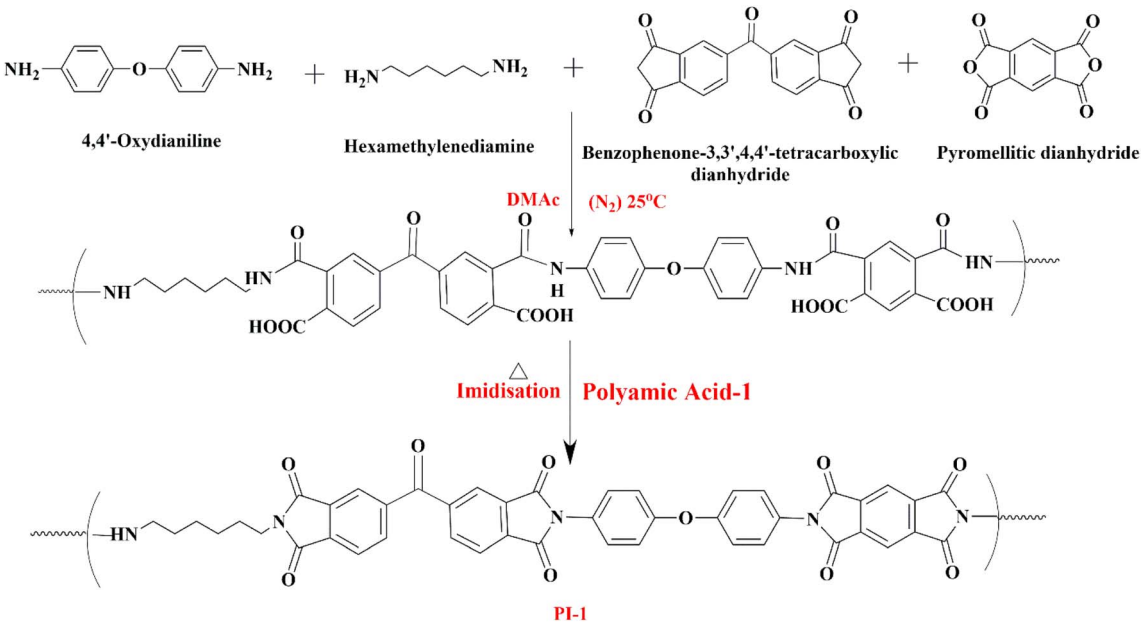

Scheme 1 Proposed reaction mechanism of PI-1.

Han *et al.* synthesized PAA using an amine-quinone diamine with BTDA and coated it on iron to achieve an aminequinone polyimide coating, which exhibited superior anticorrosion properties. They reported that the anticorrosion property was associated with the occurrence of Π-electron and lone pairs of electrons on nitrogen, which made the coordinate bond with the d-orbital of iron.[21] Huttunen-Saarivirta *et al.* synthesized amine-quinone polyimide coating on galvanized (GI) steel using 4,4′-oxydianiline (ODA), pyromellitic dianhydride (PMDA) with 2,5-bis(4,4-methylene dianiline)-1,4-benzoquinone (AQMDA), which provided good corrosion resistance.[22] The presence of aromatic rings in the monomers imparts excellent thermal stability to polyimide; however, it also increases stiffness, reducing polymer chain flexibility. This restricted mobility can create microvoids, allowing aggressive corrosive ions to penetrate more easily. To address this limitation, researchers have explored various strategies, including introducing fluorinated functional groups, incorporating functional fillers, and applying surface modifications.[23–28] Nevertheless, selecting appropriate monomers remains critical for achieving superior anticorrosion performance in polyimide coatings.

This study investigates the influence of monomer structure modification on the adhesion and corrosion protection performance of polyimide coatings applied to mild steel. Three monomers were kept constant-two diamines (ODA and HMDA) and one dianhydride (PMDA)-while the fourth monomer was varied (BPDA, BTDA, and BPADA) to formulate coatings PI-1, PI-2, and PI-3, respectively. Structural, morphological, and electrochemical characteristics of these coatings were comprehensively evaluated using solid-state ^{13}C NMR, XPS, FTIR, SEM, EIS, salt spray testing (SST), impact resistance, boiling water test, pull-off adhesion, and crosshatch adhesion tests. Thermal and viscoelastic properties were assessed through thermogravimetric analysis (TGA) and dynamic mechanical analysis (DMA), with detailed results discussed in subsequent sections.

2. Experimental section

2.1. Materials

Pyromellitic dianhydride (PMDA), benzophenone-3,3′,4,4′-tetracarboxylic dianhydride (BTDA), 4,4′-oxydianiline (ODA), 4,4′-(4,4′-isopropylidenediphenoxy) bis(phthalic anhydride) (BPADA), and *N*,*N*-dimethylacetamide (DMAc) were attained from Sigma-Aldrich, India. Hexamethylene diamine (HMDA) and 4,4′-biphthalic anhydride (BPDA) were procured from TCI

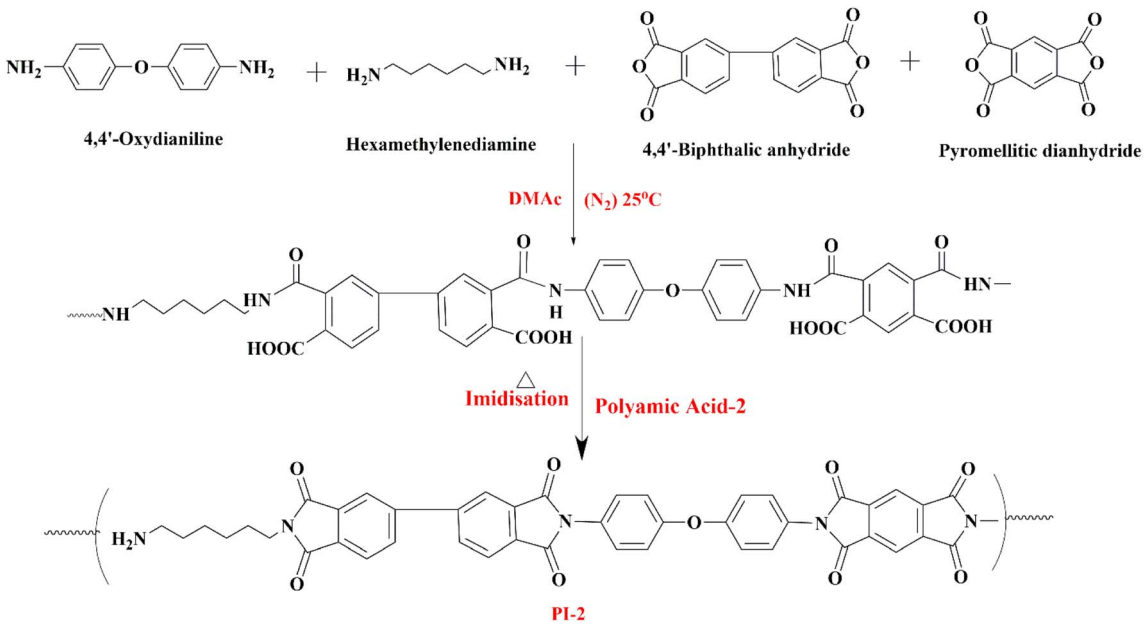

Scheme 2 Probable reaction mechanism of PI-2.

chemicals. Low-alloy mild steel sheets were collected from the CRM Tata Steel, Jamshedpur.

2.2. Methods

Three polyamic acid (PAA) coating solutions were prepared by slowly mixing the monomers (two diamines and two dianhydrides) into *N*,*N*-dimethylacetamide (DMAc) solvent and allowing them to react under an N_2 environment for 24–36 hours. Two diamines (ODA and HMDA) and one dianhydride (PMDA) have been kept constant in all three above formulations. The second dianhydride was selected out of BPDA, BTDA, and BPADA to prepare three different types of coating solutions (PAA-1, PAA-2, and PAA-3), respectively. The details of each formulation are mentioned in Table 1. The proposed possible reaction mechanisms for the formation of PAA-1, PAA-2, and PAA-3 are depicted in Scheme 1, 2, and 3, respectively.

2.3. Substrate preparation

For this study, cold-rolled close-annealed (CRCA) mild steel sheets (treated with rust preventive oil) were collected from CRM Tata Steel Limited, Jamshedpur, India. These steel sheets were cut into coupon size (10 cm × 4 cm) and degreased with an

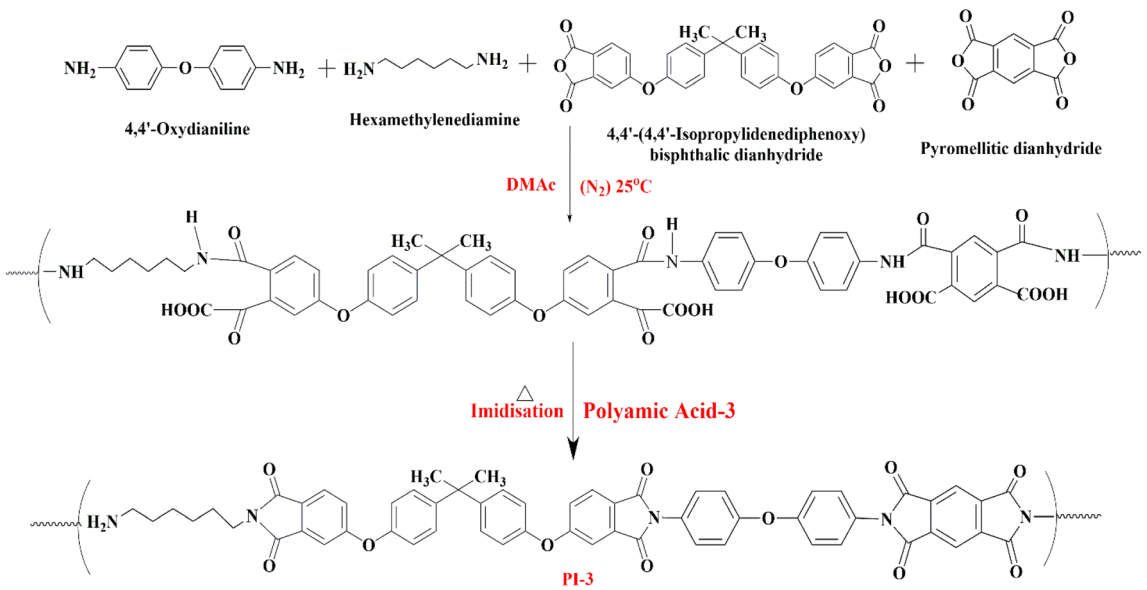

Scheme 3 Probable reaction mechanism of PI-3.

aqueous hot alkali solution to eliminate all the oil and dirt from the surface. Then, these samples were rinsed with demineralised water and dried. Finally, these samples were coated by an automated bar coater at a speed of 40 m s^{-1} to achieve a dry coating thickness of 10 ± 3 μm. The coated samples were cured at 250 °C in a hot air oven for 5 minutes to obtain the coated steels, named PI-1 for PAA-1, P-2 for PAA-2, and PI-3 for PAA-3, which were used for various characterizations and studies.

3. Characterizations

The presence of functional groups in coating solutions and on coated steel substrates was verified by FTIR spectroscopy using a Vertex 80 spectrometer (Bruker) in ATR mode within a range of 400–4000 cm^{-1}. Solid-state ^{13}C CP-TOSS (Cross-polarization with total sideband suppression) NMR spectra were obtained using a Bruker AV-500 spectrometer at a magic-angle spinning frequency of 10 kHz with a 2.5 mm rotor, to confirm the structure of the polyimide film. X-ray photoelectron spectroscopy (XPS) analysis was conducted on an Omicron ESCA system (Germany) employing a survey scan resolution of 50 eV and a high-resolution pass energy of 20 eV. The microstructural analysis of different coated steel substrates was done under an SEM (Zeiss Crossbeam 340) at a working distance of 5 mm. Electrochemical characterisations, such as potentiodynamic polarisation (Tafel) curves and electrochemical impedance spectroscopy (EIS) tests, were performed using the Gamry 1010E potentiostat instrument. It examined the corrosion resistance properties of three different types of coatings on mild steel substrates. Potentiodynamic tests were performed from −0.25 V to 0.6 V with a scan rate of 0.5 mV s^{-1}. The EIS study was conducted in the frequency range of 10^{-2} Hz to 10^{5} Hz. A three-electrode setup was employed, with the sample serving as the working electrode, having a 1 cm^2 exposed surface, the electrolyte being a 3.5% aqueous NaCl solution, the counter electrode being a platinum mesh, and the reference electrode being a saturated calomel electrode (SCE). According to ASTM B117, a salt spray test was conducted. Coupon size (10 cm × 4 cm) samples of each coating were exposed in a salt spray chamber. The coated substrates were checked at regular time intervals, and results were observed regarding changes in surface blisters, red rust, and coating failure. Dynamic mechanical analysis (DMA) was performed using a DMA 850 by TA Instruments. All tests are done with a single screw film tension clamp in temperature sweep mode, having a ramp rate of 3 °C min^{-1} up to 250 °C. Thermogravimetric analysis (TGA) was performed using a NETZSCH STA 449F3 to investigate the thermal properties of polyimide films. All experiments were conducted under an N_2 atmosphere with a heating rate of 5 °C min^{-1}, starting from 25 °C to 800 °C. A conical mandrel bend test was performed in accordance with ASTM D522 to assess the flexibility of the coating, and a pull-off adhesion test was conducted following ASTM D4541 to evaluate the coating's adhesion to the mild steel substrate. Finally, water boiling resistance was tested according to ASTM D6665 and ASTM D870 to determine the adhesion durability of the three coatings under hydrothermal conditions.

4. Results and discussion

4.1. Structural characterization

4.1.1. Fourier transform infrared (FTIR) spectroscopy. Fourier Transform Infrared (FTIR) spectroscopy is a valuable tool for analysing chemical bonding and molecular interactions of coatings. Fig. 1 shows the FTIR spectrum of PAA-1, PAA-2, and PAA-3 solutions and the coated substrates. Since the three polyimide coatings have similar functional groups, no significant changes are observed in the FTIR spectra. The formation of polyimide coatings from polyamic acid (PAA) solution leads to shifting the peak towards a higher wavelength. Due to the ODA moiety in the PAA solution, the C–O peak was observed at 1233 cm^{-1}. C=C and symmetric –CONH, asymmetric –CONH bond stretching were observed at 1497 cm^{-1}, 1635 cm^{-1}, and 1720 cm^{-1} for PI-1, PI-2, PI-3 PAA solution, which shifted to 1502 cm^{-1}, 1699 cm^{-1}, and 1770 cm^{-1}, respectively, after curing/imidization.[29,30] Furthermore, the Fe–O–C peak was observed at 550 cm^{-1}. The reduced intensity of the C–O bond and the peak shifts confirm the interaction between the polyimide and the mild steel substrate.[31] The C–N peaks at 1393 cm^{-1} have disappeared in all PAA solutions after curing, and a new peak has been detected at 1365 cm^{-1}. The mentioned peaks confirm the successful formation of the PI

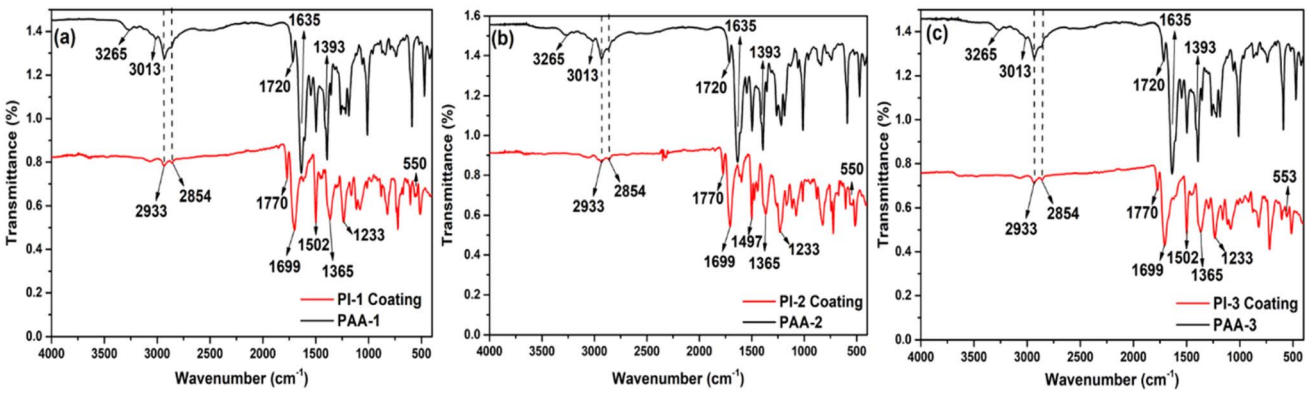

Fig. 1 FTIR spectra of (a) PI-1, (b) PI-2, (c) PI-3 polyamic acid solution and coating on mild steel.

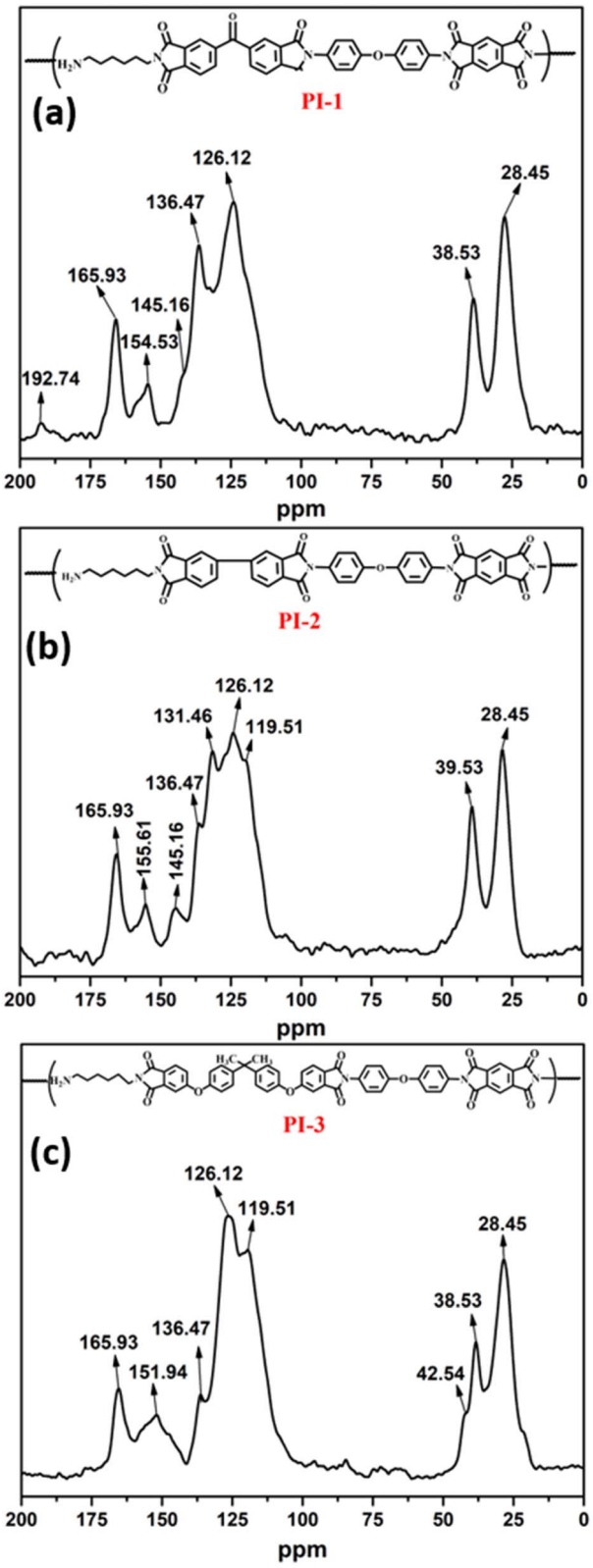

Fig. 2 Solid-state ^{13}C NMR spectra of (a) PI-1, (b) PI-2, and (c) PI-3 polyimide film.

coating on the mild steel. The peaks at 2854 cm^{-1} and 2933 cm^{-1} are also attributed to symmetric and asymmetric –CH stretching.[32] Lastly, the peaks at 3013 cm^{-1} and 3072 cm^{-1} represent various amines.[33]

4.1.2. Solid state ^{13}C NMR. Solid-state ^{13}C NMR analysis was carried out on polyimide films PI-1, PI-2, and PI-3 to confirm their molecular structures. The spectra for the three polyimides are presented in Fig. 2, and the corresponding peak assignments are summarized in Table 2. The solid-state ^{13}C NMR results clearly indicate the formation of the imide backbone and the successful incorporation of all monomeric components. All three polyimides exhibit a strong resonance at 165.9 ppm, attributed to the imide carbonyl carbons, which signifies complete cycloimidization. In PI-1 and PI-2, a resonance at 155.6 ppm corresponds to quaternary aromatic carbons bonded to heteroatoms, particularly ether-linked or imide-adjacent carbons within the aromatic rings.[34–36] In PI-3, this signal appears downfield at 151.9 ppm, likely due to the electronic influence of the bulky BPADA dianhydride. The isopropylidene bridge in BPADA modifies electron density and introduces steric effects, shifting the aromatic quaternary carbon environment to a slightly more shielded region.

A distinct resonance near 145.2 ppm in PI-1 and PI-2 is characteristic of aromatic carbons directly bonded to imide nitrogen, consistent with literature reports on rigid polyimide structures.[37–39] In PI-1, an additional peak at ~192.7 ppm corresponds to the benzophenone carbonyl (C=O) of the BPDA moiety, confirming successful incorporation of the benzophenone-containing dianhydride. A peak at 136.47 ppm, observed in PI-1, PI-2, and PI-3, is assigned to phenyl carbons in the polyimide backbone, indicating the presence of ODA, PMDA, and BPDA/BTDA/BPADA units. Two peaks at 124.3 and 119.5 ppm represent protonated and non-protonated aromatic carbons distributed across PMDA, BPDA, and ODA-based regions.[40,41] In the aliphatic region, resonances at 38.8 ppm and 27.7 ppm arise from methylene units of the HMDA segment-the former from CH_2 carbons bonded to nitrogen and the latter from internal aliphatic methylene groups-confirming incorporation of the flexible HMDA component.[42–44] Overall, the chemical shift distribution aligns with the expected structures of PI-1, PI-2, and PI-3, demonstrating well-defined, fully imidized polyimide networks.

4.1.3. X-ray photoelectron spectroscopy (XPS) analysis. High-resolution X-ray photoelectron spectroscopy (XPS) measurements of the C 1s, N 1s, and O 1s regions were performed to understand the chemical environments and the influence of different dianhydride structures on the electronic characteristics of PI-1, PI-2, and PI-3 polyimide films (Fig. 3). The core-level spectra for all samples exhibit the typical features expected for fully imidized aromatic polyimides, and their deconvolution provides deeper insight into how structural variations in the monomers affect the resulting bonding states. In all samples, the C 1s, N 1s, and O 1s peaks appear broadly around ~284 eV, ~399 eV, and ~531 eV, respectively, consistent with the literature for aromatic imide systems. Upon peak fitting, the C 1s region (Fig. 3a, d and g) resolves into several components positioned at ~283.1–283.3 eV (C–C), ~284.0 eV

Table 2 Peak assignments in the solid-state ^{13}C NMR spectra of PI-1, PI-2, and PI-3 polyimide films

Peak (ppm)	Sample details	Observation
28.45	PI-1, PI-2, PI-3	Aliphatic carbon within the polymer backbone
38.53	PI-1, PI-2, PI-3	($-CH_2$)methylene, ($-CH$) methine carbons in aliphatic region
42.54	PI-3	Aliphatic quaternary carbon
119.51	PI-1, PI-2, PI-3	Aromatic C–H in the polymer backbone
126.12	PI-1, PI-2, PI-3	Amine imide C–N
136.47	PI-1, PI-2, PI-3	Carbon present in the phenyl group of the polyimide backbone
145.16	PI-1, PI-2	Aromatic carbon atom within the polymer's backbone or side group (N)
155.61	PI-1, PI-2, PI-3	Quaternary aromatic carbon atom bonded to an O or N atom
165.93	PI-1, PI-2, PI-3	Carbon atom of the C=O group in the imide ring
192.47	PI-1	Benzophenone C=O (ketone)

(C–N), ~284.6 eV (C–N–C), ~284.8–285.3 eV (C–O), ~287.3–287.8 eV (C=O), and ~288.3–288.6 eV (imide N–C=O).[45,46] These peaks collectively confirm the successful formation of the imide rings and the presence of aromatic and heteroatom-linked carbons throughout the polymer backbone. The N 1s spectra (Fig. 3b, e and h) further support this conclusion, showing distinct contributions at ~398.3–398.5 eV (N–C), ~398.6–399.0 eV (N–H), and ~399.5–400.5 eV (imide N–C=O). The presence of the imide N–C=O peak is a clear indicator of complete cyclodehydration during imidization.[47,48] The O 1s

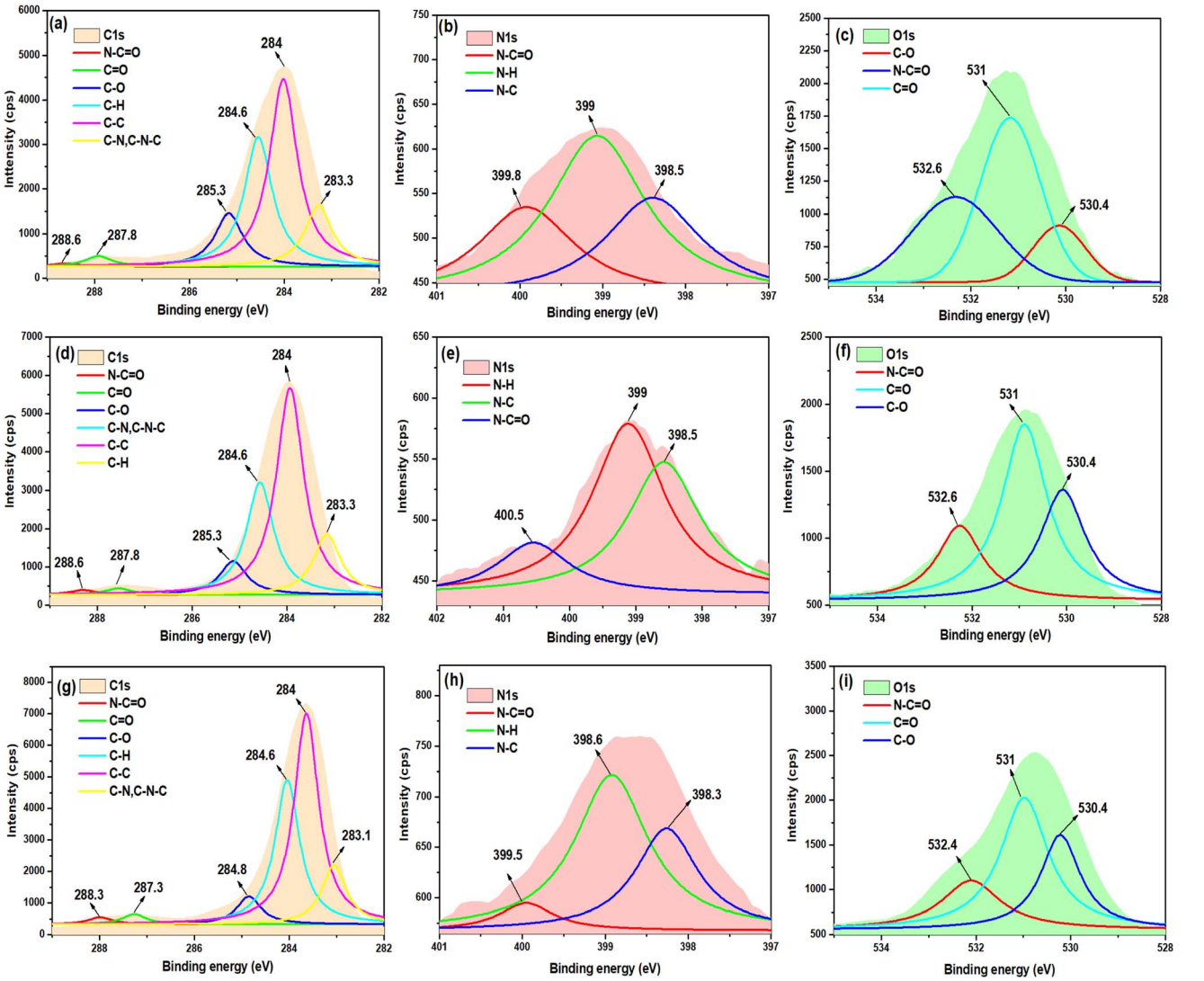

Fig. 3 Deconvoluted XPS spectra of (a) C 1s, (b) N 1s, and (c) O 1s for PI-1; (d) C 1s, (e) N 1s, and (f) O 1s for PI-2; and (g) C 1s, (h) N 1s, and (i) O 1s for PI-3 polyimide films.

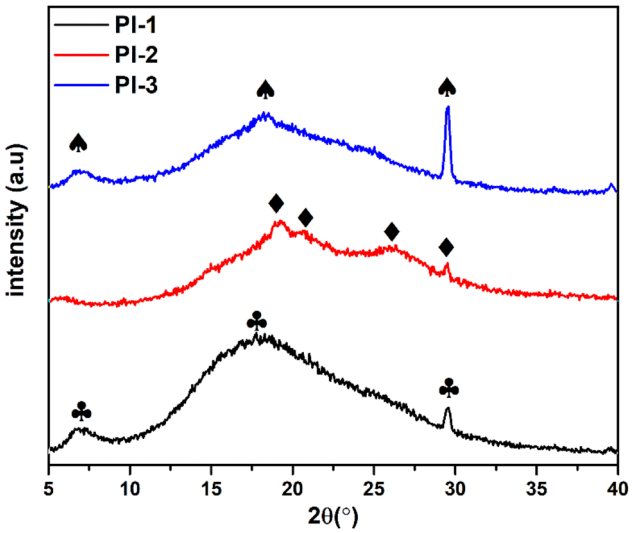

Fig. 4 XRD spectra of PI-1, PI-2, and PI-3 films.

spectra (Fig. 3c, f and i) exhibit peaks at ~530.4 eV (C–O), ~531.0 eV (C═O), and ~532.4–532.6 eV (imide N–C═O oxygen). Together, these oxygen species reflect the coexistence of ether oxygen (from diamines), carbonyl oxygen, and imide oxygen atoms within the polymer structure.[49–51] A significant observation among the three samples is the alteration in binding energies for carbonyl-related peaks in PI-3 compared to PI-1 and PI-2. Specifically, the C═O and N–C═O peaks of PI-3 appear at slightly lower binding energies, suggesting a higher local electron density on the carbonyl groups. This shift is attributed to the BPADA dianhydride, which contains bulky bisphenol-A units with electron-donating characteristics. These groups increase the electron density on adjacent atoms and reduce the effective core-level binding energy. In contrast, BPDA and BTDA in PI-1 and PI-2 contain more rigid and more electron-withdrawing aromatic units, resulting in slightly higher binding energies. The XPS study confirms the complete imidization of all three polyimides and reveals that changes in the structure of the dianhydride monomer have a significant impact on the electronic environment, particularly around carbonyl and imide functional groups.

4.1.4. Wide-angle X-ray diffraction (WAXD) analysis. An X-ray diffraction (XRD) study was conducted to elucidate the crystalline structure, phase composition, and polymer interactions within the polyimide coating matrix. A wide-angle X-ray diffraction (WAXD) characterized the crystalline and amorphous nature of polyimide film, and the patterns obtained are shown in Fig. 4. Broadest peaks are observed for PI-1 and PI-2, indicating the amorphous nature of the polymer.[52] In contrast, some sharp peaks are observed in the case of PI-3, suggesting semicrystalline characteristics of this polymer. The main diffraction peaks for these polymers are observed at 6.9°,18.34°, 29.5° (in case of PI-1), 19.13°, 20.8°, 26.14°, 29.5° (in case of PI-2), and 6.91°,17.78°,29.5° (in case of PI-3).

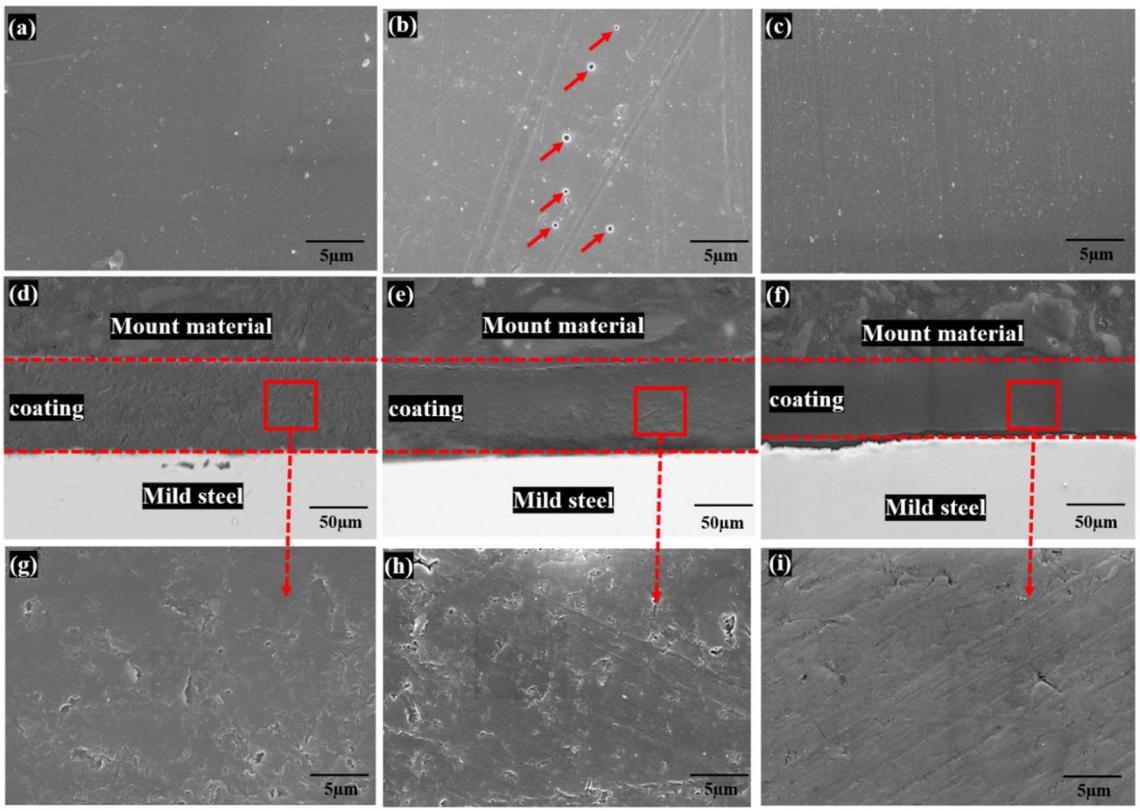

Fig. 5 SEM surface images of (a) PI-1, (b) PI-2, and (c) PI-3 coated mild steel, cross-section microstructure of (d) PI-1, (e) PI-2, and (f) PI-3 coating and magnified cross-section images of (g) PI-1, (h) PI-2, and (i) PI-3 coating.

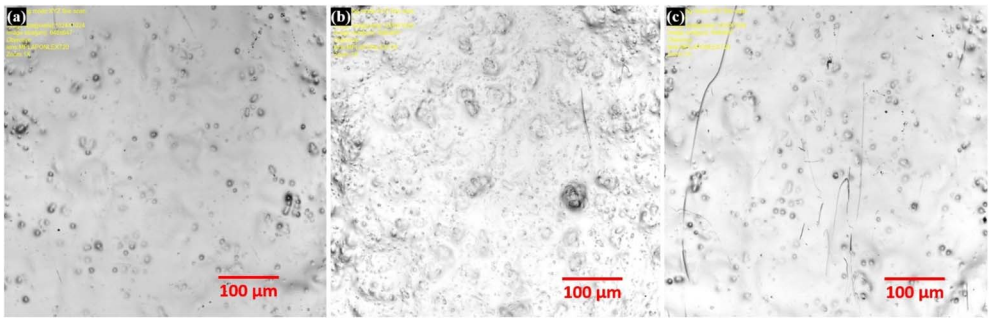

Fig. 6 CLSM images of (a) PI-1, (b) PI-2, and (c) PI-3 coated mild steel.

The mentioned peaks correspond to *d*-spacings of 1.27 nm, 0.498 nm, 0.302 nm (for PI-1), 0.461 nm, 0.425 nm, 0.3411 nm, 0.3035 nm (for PI-2), and 1.27 nm, 0.4848 nm, 0.3035 nm (for PI-3), demonstrating its structural property as well as the intermolecular regularity. The crystalline nature of PI-3 polymer helped achieve greater mechanical and corrosion resistance properties, which are discussed further.

4.2. Coating microstructure

4.2.1. Scanning electron microscopy. The scanning electron microscopy (SEM) technique is used to study the surface morphology, topography, and composition of the coated steel substrates. The surface and cross-section morphology of PI-1, PI-2, and PI-3 coatings have been shown in the figure (Fig. 5a–f). It is evident from the surface morphology that all the coatings were smooth and defect-free on PI-1 and PI-3. However, some pores were found on PI-2, which formed during the solvent evaporation process. The corroding ions penetrated through these pores, which resulted in the low anticorrosion property of PI-2.

On the other hand, the cross-section images revealed three distinct morphologies resulting from the varying crosslinking densities of the three different anhydrides present in the polyimide system. Moreover, the PI-3 cross-section showed a smoother and more compact microstructure than PI-1 and PI-2. DMA and impact tests further verified the compactness and strength of the three coatings.

4.2.2. Confocal laser scanning microscopy (CLSM). The Confocal Laser Scanning Microscopy (CLSM) 2D images were taken to check the surface morphology and roughness of PI-1, PI-2, and PI-3 polyimide-coated mild steel substrates. The obtained images are shown in the figure (Fig. 6). CLSM images confirm that PI-1 and PI-3 exhibited relatively smoother surfaces, but PI-2 revealed a coarser structure. Furthermore, the obtained average roughness (Ra) for PI-1, PI-2, and PI-3 are 0.368 μm, 0.391 μm, and 0.356 μm, respectively. PI-2 showed the highest roughness of 0.391 μm due to the presence of holes, which were formed due to the evaporation of solvent. However, the smoother surface of PI-3 confirms the formation of a superb barrier network of polyimide on mild steel, leading to the best anticorrosion performance among all coatings.[53,54]

4.3. Electrochemical characterization

4.3.1. Potentiodynamic polarization study. The corrosion resistance characteristics of three synthesized polyimide coatings were studied in a 3.5% NaCl solution using potentiodynamic polarization and electrochemical impedance spectroscopy (EIS) measurements. The electrochemical parameters of coatings, *e.g.*, corrosion rate, anodic Tafel slope (βa), cathodic Tafel slope (βc), corrosion potential (E_{corr}), and corrosion current density (I_{corr}) and the goodness of fit (Chi squared) values are calculated using the Tafel extrapolation method, and the exported data are given in Table 3. The observed chi-squared value for all substrates is <0.05, indicating a very good fit of the data. Fig. 7a shows the Tafel plots of PI-1, PI-2, and PI-3. A decreased corrosion rate can be indicated by a low corrosion current density and a positive shift in corrosion potential values. It was found that all the coatings exhibited a higher corrosion potential than bare mild steel. However, the highest corrosion potential was observed at −0.605 mV for PI-3 coated steel, whereas the lowest corrosion potential was observed at −0.618 mV for PI-1 coated steel. Furthermore, the corrosion current density was the lowest at 0.214 nA for PI-3 coated steel. As more C=O bonds are present in PI-3, the polymer structure flexibility increases, resulting in better film formation with higher anti-corrosion properties of the coating.

Table 3 The potentiodynamic polarization fitted parameters of mild steel, PI-1, PI-2, and PI-3

Sample-ID	βa (V per decade)	βc (V per decade)	I_{corr} (nA)	E_{corr} (mV)	Corrosion rate (mpy)	Goodness of fit (Chi squared)
Mild steel	49.50×10^{-3}	162.0×10^{-3}	7850.0	−731.0	0.3578×10^{-1}	3.968×10^{-5}
PI-1	19.31×10^{-1}	917.3×10^{-3}	22.30	−653.0	1.019×10^{-4}	1.086×10^{-7}
PI-2	25.33×10^{-1}	23.36×10^{-1}	320.0	−618.0	1.463×10^{-5}	1.973×10^{-3}
PI-3	54.70×10^{-3}	278.4×10^{-3}	0.214	−605.0	9.766×10^{-7}	2.650×10^{-3}

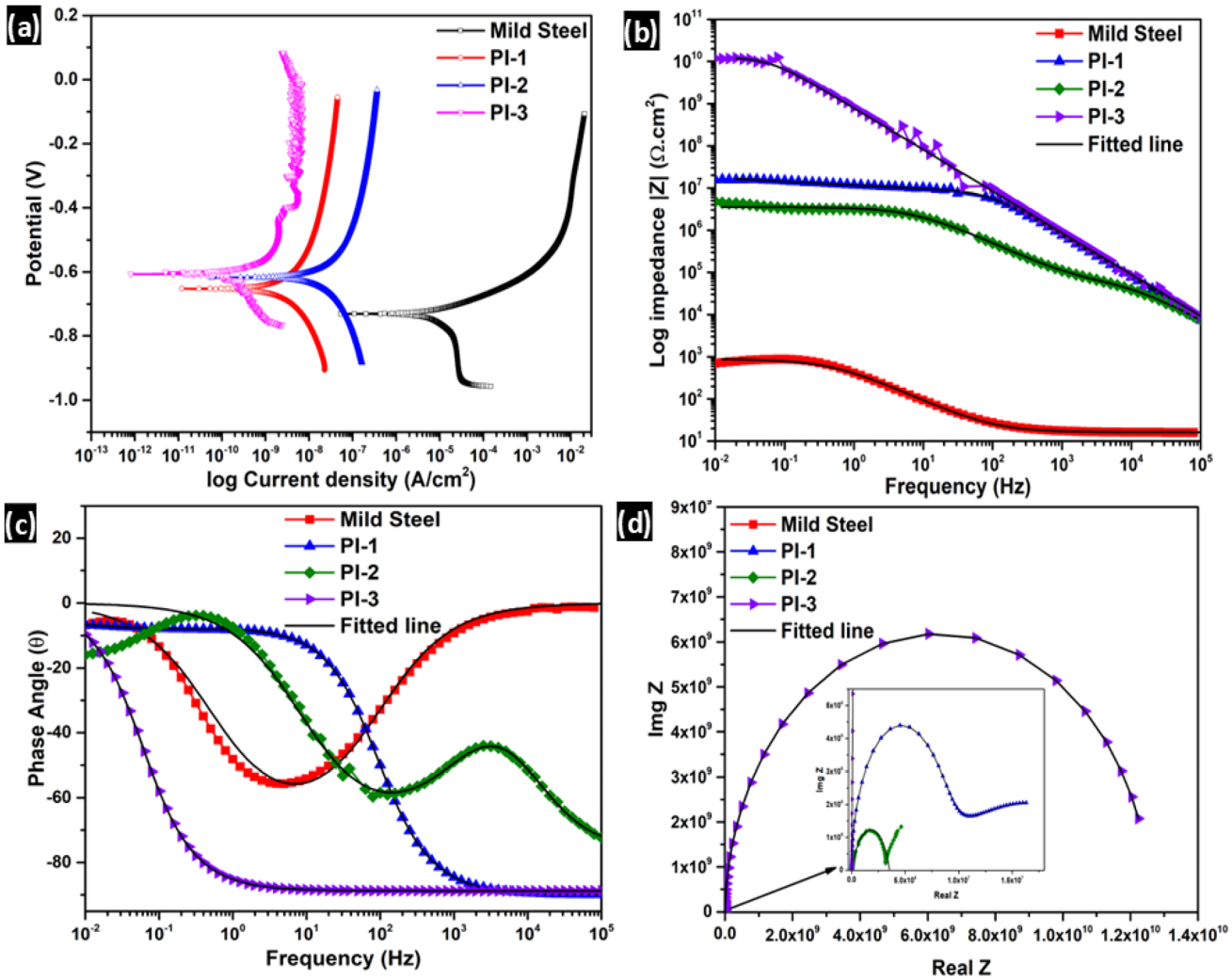

Fig. 7 (a) Potentiodynamic polarization graphs, (b) impedance plots, (c) phase angle plots, and (d) Nyquist plots of PI-1, PI-2, and PI-3 in comparison to mild steel.

The improved film formation and mechanical properties of PI-3 helped achieve better corrosion resistance, which is discussed further.

4.3.2. Electrochemical impedance spectroscopy (EIS) analysis. Electrochemical impedance spectroscopy (EIS) is a widely used and highly sensitive method for assessing the anti-corrosion ability of coatings. The barrier properties of polyimide coatings can be assessed through electrochemical impedance spectroscopy (EIS).[55] Here, we used the EIS technique to measure the impedance and phase angle of coated steel sheets (PI-1, PI-2, and PI-3), from which we plotted the Bode and Nyquist diagrams (Fig. 7b–d). The Randles equivalent circuit was used for mild steel and polyimide-coated mild steel (Fig. 8a and b), where solution resistance (R_{soln}), the resistance associated with charge transfer of electrons through the double layer (R_{ct}), capacitance of the film/coating (CPE_f/CPE_{ct}), and resistance of the film (R_f) values were calculated. Instead of a pure capacitor, a constant phase element (CPE) was applied. R_f + R_{ct} is the total resistance of the coating (R_t), and the total capacitance (C_t) is calculated by CPE_f + CPE_{ct}. The fitted Randle's circuit data is given in Table 4. As the resistance of the solution is not a material parameter, it can be negligible.[3] We

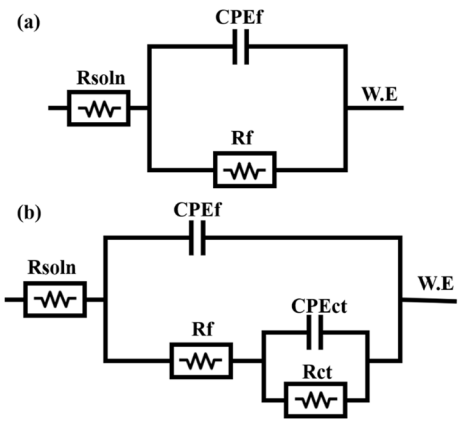

Fig. 8 Randles circuit used for fitting (a) mild Steel, and (b) PI-1, PI-2, PI-3 observed data.

Table 4 The electrochemical fitted parameters of mild steel, PI-1, PI-2, and PI-3 coating

Sample name	$R_{soln} \pm$ SD (Ω cm^2)	$R_{ct} \pm$ SD (Ω cm^2)	$R_f \pm$ SD (Ω cm^2)	$CPE_{ct} \pm$ SD (Farad)	$CPE_f \pm$ SD (Farad)	Total resistance $= R_t \pm$ SD (Ω cm^2)	Total capacitance $= C_t$ (Farad)
Mild steel	16.21 ± 0.05	NA	$8.83 \times 10^2 \pm 0.85 \times 10^2$	NA	$3.50 \times 10^{-4} \pm 1.3 \times 10^{-6}$	$8.83 \times 10^2 \pm 0.85 \times 10^2$	$3.50 \times 10^{-4} \pm 1.3 \times 10^{-6}$
PI-1	12.68 ± 0.03	$1.84 \times 10^7 \pm 2.61 \times 10^2$	$7.25 \times 10^6 \pm 6.93 \times 10^2$	$4.80 \times 10^{-7} \pm 1.21 \times 10^{-11}$	$2.05 \times 10^{-10} \pm 7.6 \times 10^{-14}$	$2.57 \times 10^7 \pm 9.54 \times 10^2$	$4.80 \times 10^{-7} \pm 1.20 \times 10^{-11}$
PI-2	14.1 ± 0.09	$3.46 \times 10^6 \pm 1.93 \times 10^2$	$7.15 \times 10^4 \pm 1.71 \times 10^1$	$4.69 \times 10^{-9} \pm 3.5 \times 10^{-13}$	$2.90 \times 10^{-10} \pm 9.3 \times 10^{-14}$	$3.53 \times 10^6 \pm 2.10 \times 10^2$	$4.98 \times 10^{-9} \pm 3.50 \times 10^{-11}$
PI-3	5.43 ± 0.06	$1.44 \times 10^6 \pm 5.42 \times 10^2$	$1.26 \times 10^{10} \pm 2.37 \times 10^3$	$5.26 \times 10^{-12} \pm 8.6 \times 10^{-14}$	$2.10 \times 10^{-10} \pm 3.7 \times 10^{-14}$	$1.26 \times 10^{10} \pm 2.91 \times 10^3$	$2.15 \times 10^{-10} \pm 1.23 \times 10^{-13}$

know that the higher the resistance of the coating, the higher the anticorrosion behaviour. In Fig. 7b, the highest resistance is observed by PI-3 coating, *i.e.*, $1.26 \times 10^{10} \pm 2.91 \times 10^3$ ohm cm^2. Alternatively, PI-1 and PI-2 coatings exhibit total resistance of $2.57 \times 10^7 \pm 9.54 \times 10^2$ ohm cm^2 and $3.53 \times 10^6 \pm 2.91 \times 10^3$ ohm cm^2, respectively. Due to the pores present in the PI-2 microstructure, as observed in Fig. 5b, it allowed the corrosive ions to enter, resulting in the lowest impedance of 4.8×10^6 ohm cm^2 at 0.01 Hz.[56] Additionally, the impedance at 0.01 Hz, 1.2×10^{10} ohm cm^2, results in the highest barrier property of PI-3. The lowest total capacitance of $2.15 \times 10^{-10} \pm 1.23 \times 10^{-13}$ farad and the highest total capacitance of $4.98 \times 10^{-9} \pm 3.50 \times 10^{-11}$ were observed by PI-3 and PI-2, respectively. Thus, it acted as a barrier against corrosive ions for the coated substrate. Furthermore, the phase angles at 10 Hz achieved by PI-1 and PI-2 are −12° and −36°, respectively, whereas mild steel exhibits a phase angle of −54°. Simultaneously, PI-3 coated steel showed the capacitive phase angle (−88°), which confirms the insulating barrier nature of the coating (Fig. 7c).[57] This insulating barrier prevents the flow of corrosive ions and reduces electrochemical reactions that lead to corrosion. The Nyquist plot of the three coatings is shown in Fig. 7d. It is evident that PI-3 coated steel has the largest semi-circle (loop), whereas PI-2 coated steel has the smallest semi-circle (loop) among the three coatings. In the Nyquist plot, the surface coating or film impedance determines the high-frequency loop, while the metal influences the low-frequency loop. Additionally, it can be noticed that the tail at the Nyquist plot of PI-1 and PI-2 started moving towards 45°, which could be due to the diffusion of electrolytes into the coating.[58] However, in PI-3 coated steel,

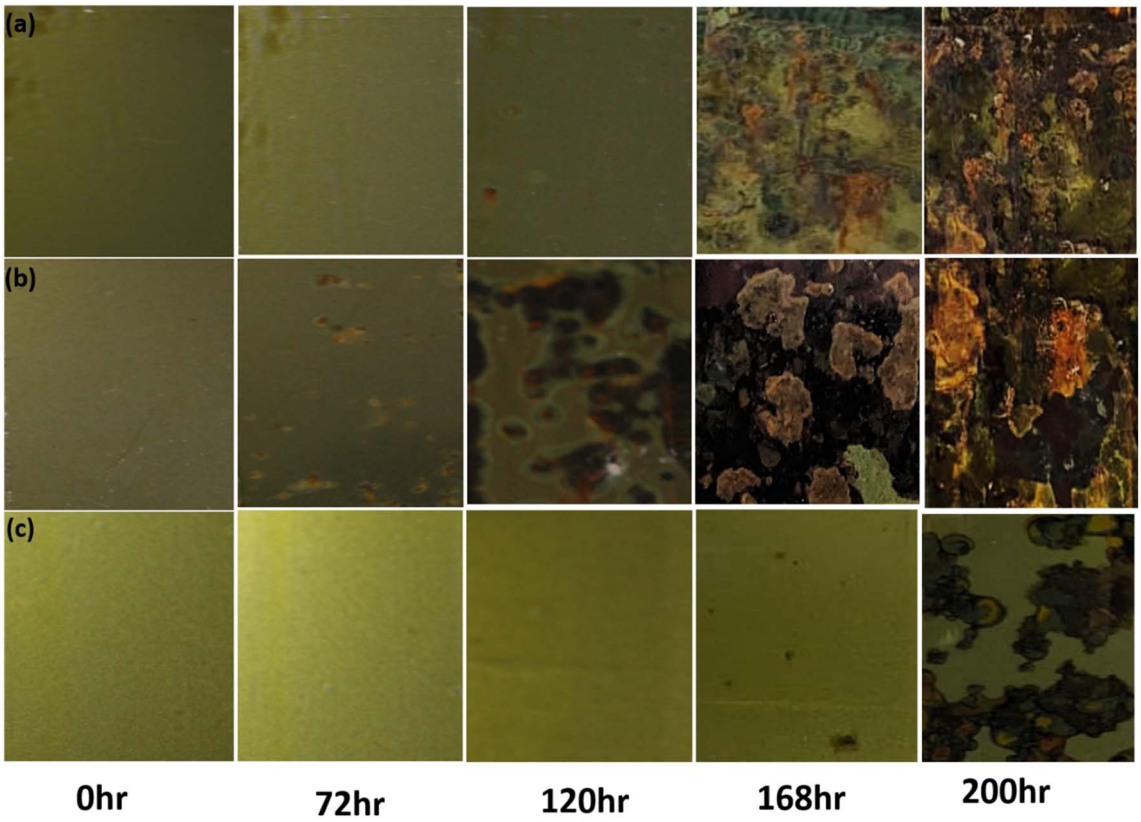

Fig. 9 SST images of (a) PI-1, (b) PI-2, and (c) PI-3 coated mild steel.

a complete semicircle has formed, which indicates the barrier property of PI-3. The dense, compact film of PI-3 acted as a barrier and helped to achieve superior corrosion resistance.

4.4. Salt spray test (SST)

The neutral salt spray test (SST) is a broadly applied accelerated corrosion testing method to evaluate the durability and effectiveness of anticorrosion coatings under harsh environmental conditions. The SST was performed as per ASTM B117 on PI-1, PI-2, and PI-3 coated steel substrates, and results were observed as coating delamination and red rust at 24-hour intervals (Fig. 9).

The salt spray pictures revealed that the first red rust spots were visible for PI-1 and PI-2 at 120 h and 72 h, respectively. The earlier red rust formation on PI-2 is due to pores in its microstructure (Fig. 5b). Conversely, there is no sign of red rust till 168 h in the case of PI-3 coated steel. After 200 hours, PI-1-coated steel exhibited around 70% red rust, whereas in the case of PI-2 coated steel, coating delamination was observed in some places. This occurred due to the amorphous nature of the PI-1 and PI-2 coatings. However, PI-3 coated steel exhibits good barrier properties, which helped achieve good anticorrosion properties by displaying very few rust spots after 200 hours of exposure in a 5% NaCl salt fog environment. The above SST analysis supports the EIS and potentiodynamic results.

4.5. Coating robustness and adhesion test (impact and crosshatch test)

The robustness of the coating was evaluated through an impact test, while its adhesion to the steel substrate was assessed using the crosshatch test. The formability and adhesion properties of three coated steels (PI-1, PI-2, and PI-3) were evaluated through impact and crosshatch tests, respectively. The obtained optical micrographs after the impact test are shown in Fig. 10.

It is clear from the image that all the samples passed the above tests. However, when closely observed, microcracks were formed on PI-1 and PI-2, but there is no sign of cracks on PI-3. It has retained its initial crack-free structure. This occurred due to the excellent adhesion, high crosslinking density, and increased ether linkages in the BPADA-based coating (PI-3), which enhanced the flexibility of the PI-3 coating. Moreover, the crosslinking density of the coating was further verified by DMA, as presented in section 4.8. The coating adhesion test was performed using a crosshatch test in accordance with the ASTM

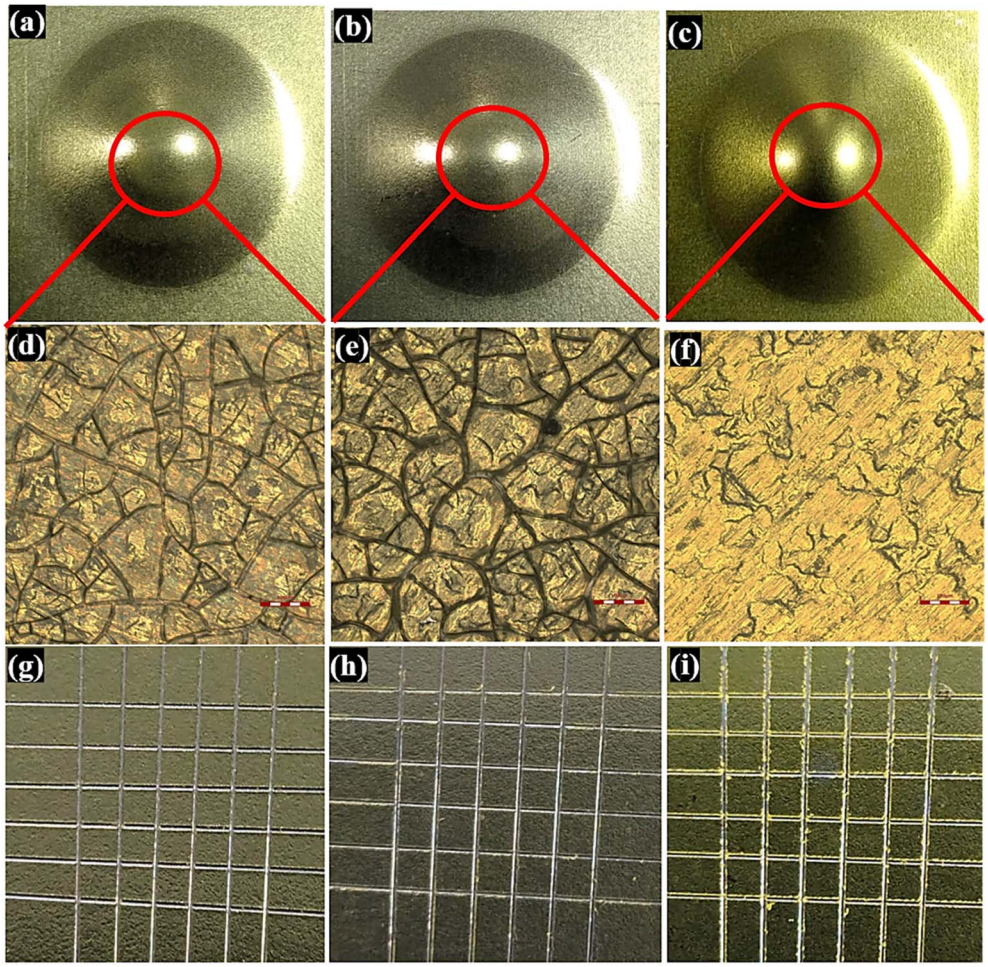

Fig. 10 Optical images of (a) PI-1, (b) PI-2, and (c) PI-3 after impact test, magnified CLSM images of impact portion of (d) PI-1, (e) PI-2, and (f) PI-3, crosshatch adhesion results for (g) PI-1, (h) PI-2 and (i) PI-3.

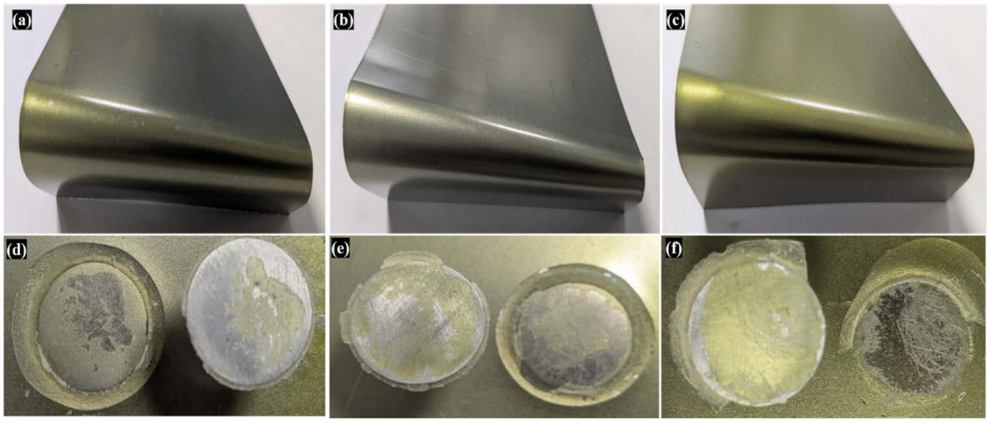

Fig. 11 Conical mandrel bend test results for (a) PI-1, (b) PI-2, and (c) PI-3; and pull-off adhesion tested samples of (d) PI-1, (e) PI-2, and (f) PI-3 on coated mild steel substrates.

D6677 standard. It was found that the edges of the cuts were entirely smooth, and no squares were detached by passing the test with the 5B classification.[59] This occurred due to the absorption of the C–O bond, the –OH stretching vibration, and the shifting of the C═O peak in the coating, confirming the formation of the Fe–O–C bond, which has further contributed to achieving superior adhesion.

4.6. Conical mandrel and pull-off adhesion tests

The PI-1, PI-2, and PI-3 polyimide-coated metal substrates were subjected to the conical mandrel bend test (Fig. 11a–c), which measures the coating's resistance to cracking or detachment under mechanical deformation, in compliance with ASTM D522 and ISO 6860 standards. The assessment of the coating's resistance to cracking or separation under mechanical deformation is done by bending the coated panels over a conical mandrel. The bend test was done on all samples, with each coated panel being bent over the conical mandrel to a specific angle.[60,61] After that, a careful visual assessment of the bent portions revealed that none of the samples exhibited fractures, delamination, or flaking. It appears that there is no damage to the surface or separation of the coating at the bend area, indicating that all three coatings are very flexible and adhere well to the substrate. As a result, all the samples passed the conical mandrel test, indicating that they were mechanically dense and could be used in situations where deformation resistance was required.

To further complement the conical mandrel test of the coating, a pull-off adhesion test was conducted on PI-1, PI-2, and PI-3 coatings in accordance with the ASTM D4541 and ISO 4624 standards. The images obtained after the tests are shown in Fig. 11d–f. Typically, three forms of rupture are observed during the adhesion test of coatings: adhesive failure, half-cohesive failure, and cohesive failure. In adhesive failure, the coating exhibits significant strength, remaining intact and fully bonded to the substrate. In half-cohesive failure, fifty percent of the coating detaches from the substrate while the other fifty percent stays adhered. In cohesive failure, the coating is fully bonded to the substrate; however, damage arises from a rupture inside the coating itself.[24,62] All polyimide-coated samples demonstrate a third mode of rupture, characterized by the adhesion strength of the coatings surpassing the cohesive strength. This leads to the coating's failure to endure the applied perpendicular force during the pull-off test, ultimately resulting in rupture through the inner layer of the coating. The obtained adhesion strengths of PI-1, PI-2, and PI-3 are 2.45 MPa, 1.87 MPa and 3.03 MPa, respectively. This suggests that PI-3-coated steel exhibited the highest adhesion strength than PI.

4.7. Boiling water test

The coating adhesion test was additionally examined using the boiling water test at approximately 100 °C. The boiling water test conducted on PI-1, PI-2, and PI-3 coated steel assesses the coating's durability against the impacts of extended exposure to boiling water. This assessment evaluates whether the coating will preserve its adhesion and visual quality after exposure to these conditions. The assessment can determine whether the coating is prone to blistering, cracking, peeling, or other types of deterioration when exposed to hot water. Boiling water simulates scenarios in which coated steel may encounter elevated temperatures and humidity, like those found in specific industrial or marine environments. A 2/3rd portion of the samples, specifically those coated with PI-1, PI-2, and PI-3, both with and without crosshatch, underwent immersion in boiling water at approximately 100 °C for a period of 1 hour (Fig. 12 and 13). Following the immersion, the samples were extracted and allowed to cool. The coating was thereafter subjected to visual inspection for alterations such as blistering, cracking, peeling, and discolouration.[63,64]

No alterations to the coatings, such as blistering, cracking, or peeling, were detected (Fig. 12g–i). The adherence of the coating after immersion was assessed by attaching adhesive tape to the coated surface and subsequently removing it to determine if the coating had separated from the steel. The absence of coating delamination (Fig. 13g–i) following the boiling water test suggests that the PI-1, PI-2, and PI-3 coated polyimide coating exhibits robust adherence to mild steel substrates with 5B classification.

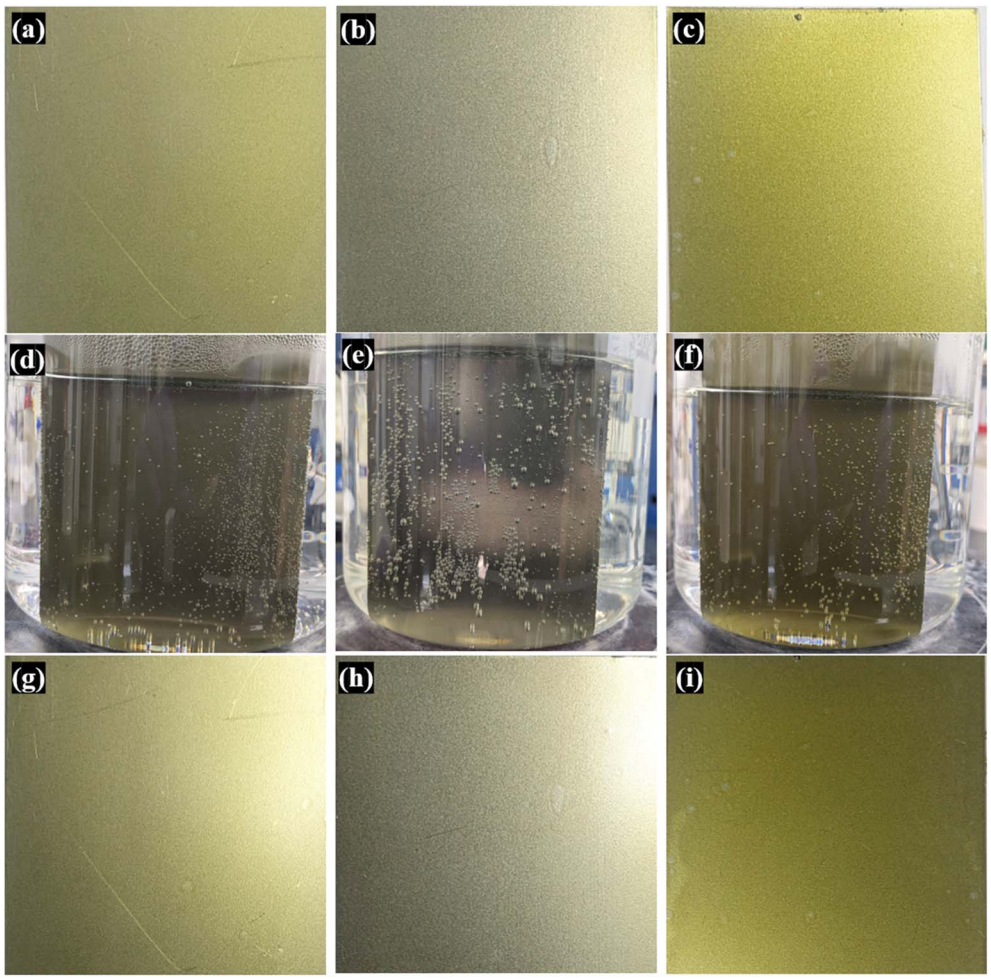

Fig. 12 Digital images of (a) PI-1, (b) PI-2, (c) PI-3 coated mild steel before the hot water test, during the hot water test of (d) PI-1, (e) PI-2, (f) PI-3, and after the hot water test of (g) PI-1, (h) PI-2, and (i) PI-3 coated mild steel.

4.8. Dynamic mechanical analysis (DMA)

Dynamic mechanical analysis (DMA) provides a comprehensive understanding of coating films' mechanical and thermal behaviour, making it indispensable for optimizing their formulation and performance. The viscoelastic properties of PI-1, PI-2, and PI-3 polyimide films were examined by a dynamic mechanical analyser (DMA). The polyimide films were obtained by step curing at 80 °C, 140 °C, 180 °C, and 250 °C for 2 h, 3 h, 1 h, and 30 minutes, respectively. The films were cut into 6 cm × 0.5 cm × 0.65 mm ($l \times w \times t$) for testing, and the storage modulus (E'), loss modulus (E'') and a measure of dissipation or damping (tan δ) at 1 Hz oscillatory deformation were recorded between the temperature ranging from 25 °C to 250 °C. The plotted graphs are shown in Fig. 14, and the exported values are given in Table 5.

The crosslinking density of three polymers is evaluated by the equation:[65]

$$C_d = \frac{E'}{3R(T_g + 40)} \quad (1)$$

where C_d = Crosslinking density per unit volume (mol m^{-3}). E' = Storage modulus in the rubbery plateau (MPa). R = Universal gas constant (8.314 J K^{-1} mol^{-1}) and T_g = Glass transition temperature E' and E'' values are dependent on temperature and progressively decrease with an rise of temperature.[66] The observed E' values for PI-1, PI-2, and PI-3 at 25 °C are 1240 MPa, 1915 MPa, and 1780 MPa, respectively (Fig. 14a).

The highest E' value of PI-2 is due to increased crystallinity and stiff BPDA structure.[67] On the other hand, due to the ether linkage in BTDA and BPADA, their storage modulus decreased significantly. However, the same ether linkage provided flexibility to PI-3, thus resulting in the highest E'' of 297.46 MPa at 25 °C. Fig. 14c shows the tan δ graphs of the damping spectra of three polyimide films. It is revealed that when the temperature rises, damping reaches a maximum in the transition area before decreasing in the rubbery region. Damping is minimal below T_g because the chain fragments are immobilized.[68] The observed tan δ values for PI-1, PI-2, and PI-3 are 0.038, 0.042, and 0.177, respectively. PI-3 showed the highest damping characteristic among the three polyimides. The T_g values for PI-1, PI-2, and PI-3 are observed at 183 °C, 220 °C, and 178 °C respectively. PI-2 achieved the highest glass transition temperature. The rigidity in BPDA restricts chain mobility and enhances thermal stability, a property further discussed in the TGA study.

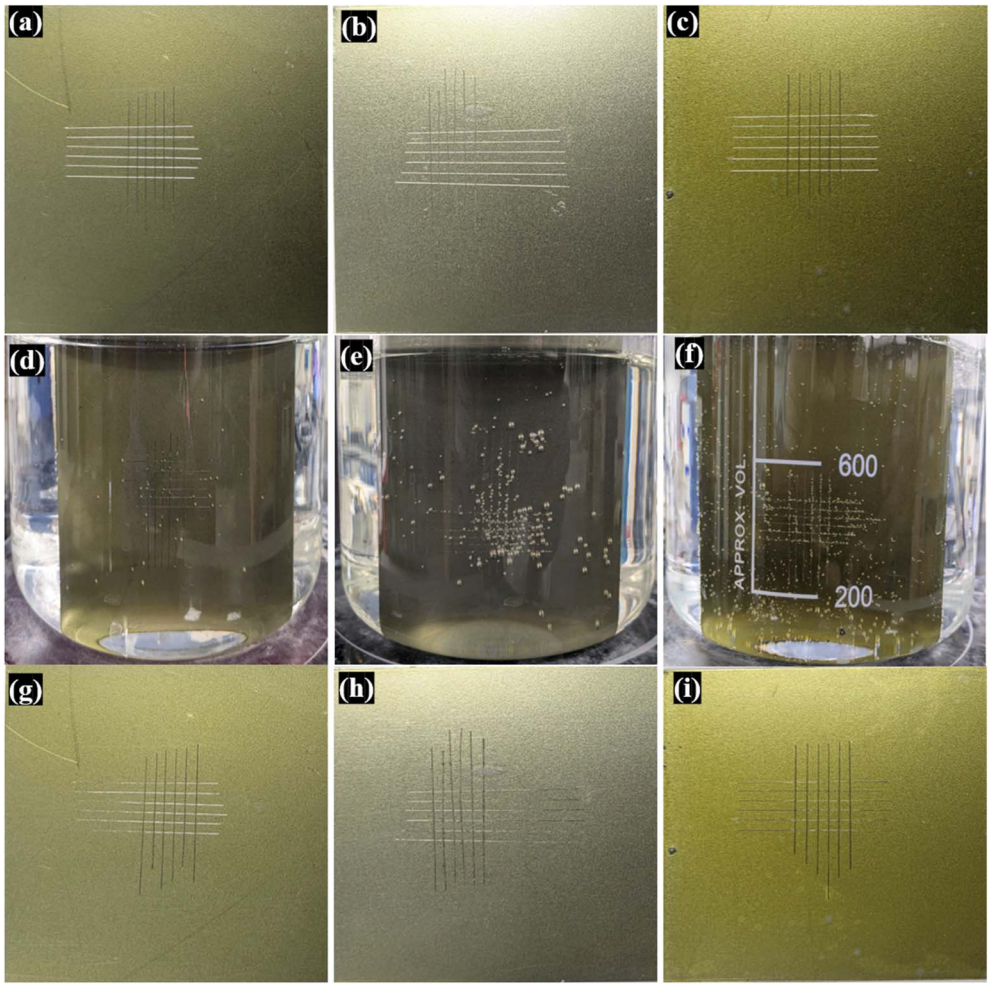

Fig. 13 Digital images of cross-cut marked coated mild steel samples: (a) PI-1, (b) PI-2, and (c) PI-3 before the hot water test; during the test for (d) PI-1, (e) PI-2, and (f) PI-3; and after the test for (g) PI-1, (h) PI-2, and (i) PI-3.

4.9. Thermogravimetric analysis (TGA)

The thermal consistency, decomposition behaviour, and material composition of polymers can be evaluated by Thermogravimetric Analysis (TGA). The thermal behaviour of PI-1, PI-2, and PI-3 polyimide coatings was investigated by TGA and is shown in Fig. S1 (SI). TGA curves of polyimides show the removal of physically adsorbed moisture within the initial temperature range of 50 °C to 150 °C, accompanied by a weight loss of 2–3%. After that, a distinct degradation line can be visualised from 230 °C due to the different glass transition temperatures. PI-2 contains BTDA, the most rigid structure among the three dianhydrides. The more rigid, aromatic structure enhances thermal stability.[69] On the other hand, PI-3

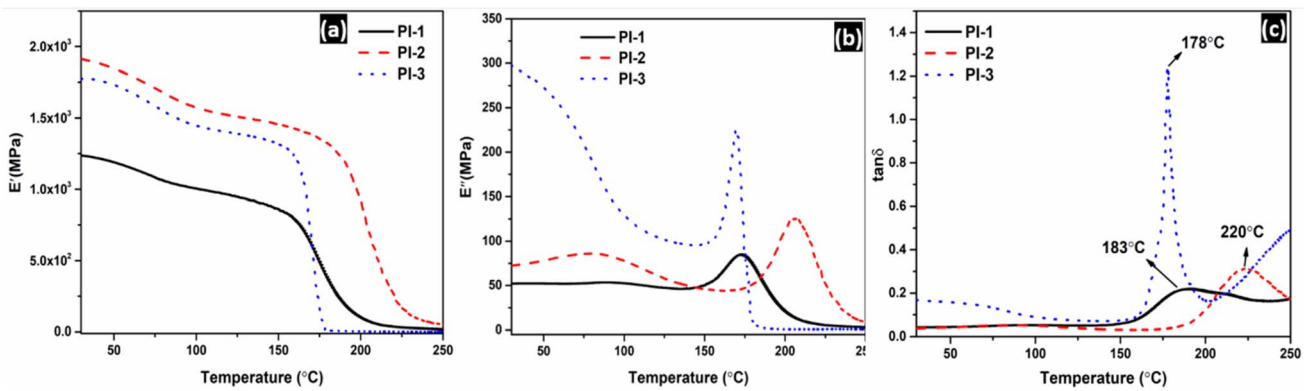

Fig. 14 (a) Storage modulus E', (b) loss modulus E'', (c) tan δ graphs of PI-1, PI-2 and PI-3 polyimide films.

Table 5 Dynamic mechanical analysis (DMA) data

Sample-ID	Storage modulus E' (MPa)	Loss modulus E'' (MPa)	tan δ	T_g Glass transition temperature (°)	C_d crosslinking density (mol m^{-3})
PI-1	1240	31.25	0.038	183	0.223
PI-2	1915	74.15	0.042	220	0.295
PI-3	1780	297.46	0.177	178	0.343

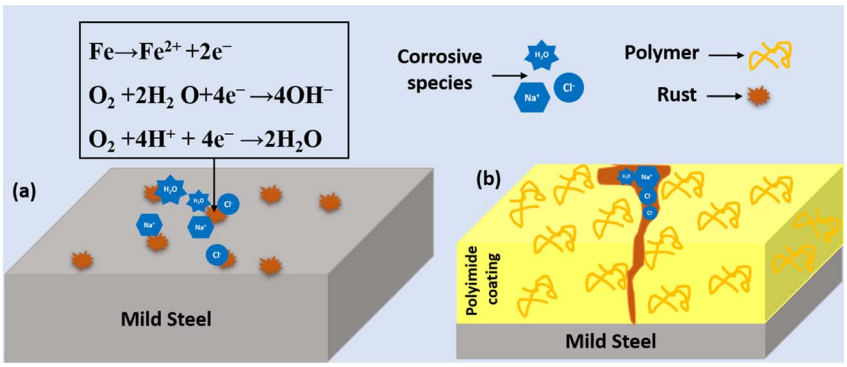

Scheme 4 Corrosion protection mechanism for (a) mild steel, and (b) PI-3 coated mild steel.

has more ether linkages, which results in reduced thermal stability compared to PI-2. So, 5% weight loss has been observed at 320 °C for PI-3, whereas 2.5% and 2% weight loss took place for PI-1 and PI-2, respectively. Severe degradation was noticed post 450 °C for PI-1, whereas it occurred for PI-2 and PI-3 after 460 °C. This difference in decomposition temperature is due to the structural change in the 2nd dianhydride molecule.

4.10. Anticorrosion mechanism

Based on the electrochemical study, a corrosion protection mechanism for PI-3 is illustrated in Scheme 4. Typically, uncoated mild steel undergoes corrosion due to electrochemical reactions with corrosive species (Na^+, Cl^-, OH^-) present in the electrolyte (Scheme 4a). In contrast, the polyimide coating significantly retards the corrosion process by acting as a barrier to these ions, preventing their penetration into the substrate (Scheme 4b).[70–72]

5. Summary and conclusion

In this work, three polyimide coating systems (PI-1, PI-2, and PI-3) were synthesized by varying the second dianhydride (BPDA, BTDA, and BPADA) while maintaining a common diamine and PMDA backbone. Comprehensive structural characterization using FTIR, XPS, and solid-state ^{13}C NMR confirmed successful imidization, the incorporation of each monomeric unit, and clear differences in the local bonding environment induced by the different dianhydride chemistries. XRD analysis revealed that PI-1 exhibited an amorphous morphology, whereas PI-2 and PI-3 displayed semicrystalline features, which influenced their mechanical behaviour. PI-1, despite its rigid aromatic structure, exhibited the lowest storage modulus, while PI-3 showed the highest crosslinking density (0.343), loss modulus (297.46 MPa), and tan δ (0.177). This is attributed to the flexible ether-rich BPADA structure, which enhances chain mobility and viscoelastic response. The improved mechanical compliance of PI-3 translated directly into superior corrosion-resistance performance. PI-3 demonstrated the most favourable electrochemical performance, with an E_{corr} of −605 mV, the highest total resistance of $1.26 \times 10^{10} \pm 2.91 \times 10^{3}$ ohm cm^2, and complete suppression of rust formation for up to 168 hours. Adhesion evaluations, including conical bend, cross-hatch, boiling water, and pull-off tests, further confirmed its exceptional interfacial stability. The highest pull-off adhesion strength (3.03 MPa) observed for PI-3 is attributed to the formation of Fe–O–C bonds at the polymer–steel interface, which significantly enhanced interfacial bonding. This strong adhesion is a key factor enabling the outstanding barrier protection delivered by the BPADA-based coating. Thermal analysis revealed contrasting trends: the flexible bisphenol-A core in BPADA reduced thermal stability in PI-3, whereas the fully aromatic, rigid BPDA unit imparted the highest thermal resistance to PI-1. Overall, the results demonstrate a clear structure–property relationship: rigid polyimide architectures enhance thermal stability, while flexible, ether-containing structures improve adhesion, mechanical damping, and corrosion protection. These insights establish a design framework for tailoring high-performance polyimide coatings to meet the demands of anticorrosion applications.

Author contributions

Sukanta Badaik: conceptualization, writing – original draft, formal analysis, data curation. Suryakanta Nayak: writing – review & editing, supervision, formal analysis,

conceptualization. Balram Ambade: writing – review & editing, formal analysis. Tapan Kumar Rout: writing – review & editing, supervision, formal analysis, conceptualization.

Conflicts of interest

There are no conflicts to declare.

Data availability

All data underlying the results are available as part of the article and no additional source data is required.

Supplementary information (SI): thermogravimetric analysis (TGA). See DOI: https://doi.org/10.1039/d5ra05765e.

Acknowledgements

The authors were thankful to Tata Steel management for allowing this article to be published. We also like to thank the Ministry of Education (MoE) for providing PhD fellowship. We would like to thank Dr KSN Raju for helping with the NMR facility. Finally, we would like to express our thanks to our lab supervisors (Mrs Puja Kumari, Priti Prakash Sahoo, Rintu Ghosh and research colleagues who helped us throughout the experiment and characterization.

References

1 S. Mandal, R. Ghosh, S. Kunar, R. Samanta, A. Sinha and G. Mandal, *J. Inst. Eng. (India): Ser. D*, 2024, **105**, 2023–2038.
2 S. B. Ulaeto, R. P. Ravi, I. I. Udoh, G. M. Mathew and T. P. D. Rajan, *Corros. Mater. Degrad.*, 2023, **4**, 284–316.
3 R. Mukherjee, S. Badaik, A. K. Pandey, A. N. Bhagat and T. K. Rout, *Mater. Chem. Phys.*, 2023, **309**, 128292.
4 A. Sezer Hicyilmaz and A. Celik Bedeloglu, *SN Appl. Sci.*, 2021, **3**, 1–22.
5 I. Gouzman, E. Grossman, R. Verker, N. Atar, A. Bolker and N. Eliaz, *Adv. Mater.*, 2019, **31**, 1–15.
6 Y. Y. Liu, Y. K. Wang and D. Y. Wu, *J. Appl. Polym. Sci.*, 2022, **139**, 1–24.
7 P. Ma, C. Dai, H. Wang, Z. Li, H. Liu, W. Li and C. Yang, *Compos. Commun.*, 2019, **16**, 84–93.
8 C. Yi, W. Li, S. Shi, K. He, P. Ma, M. Chen and C. Yang, *Sol. Energy*, 2020, **195**, 340–354.
9 C. Huang, J. Liu, L. Zhao, N. Hu and Q. Wei, *Composites, Part A*, 2023, **168**, 107459.
10 H. C. Yu, S. V. Kumar, J. H. Lee, S. Y. Oh and C. M. Chung, *Macromol. Res.*, 2015, **23**, 566–573.
11 I. Mokhtari, C. Bas, C. Marestin, F. Schiets and M. Bartholin, *Eur. Polym. J.*, 2008, **44**, 832–841.
12 L. Loukotová, J. M. Dodda, P. Bělský, L. Kullová, J. Kadlec, M. Podivinská and J. Vohlídal, *J. Appl. Polym. Sci.*, 2017, **134**, 1–9.
13 G. Zhao, M. Zhang, Y. Men, M. Ding and W. Jiang, *J. Appl. Polym. Sci.*, 2008, **108**, 1893–1900.
14 Y. Zhang, L. Qu, J. Liu, X. Wu, Y. Zhang, R. Zhang, H. Qi and X. Zhang, *J. Coat. Technol. Res.*, 2019, **16**, 511–520.
15 Z. Li, H. Song, M. He, J. Liu and S. Yang, *Prog. Org. Coat.*, 2012, **75**, 49–58.
16 H. Jiang, H. Zhang, Y. Wen, L. Tan, X. Fang and G. Chen, *Polymer*, 2022, **249**, 124845.
17 H. Jiang, H. Jiang, G. Chen and X. Fang, *J. Polym. Sci.*, 2021, **59**, 1434–1445.
18 M. H. Tsai, Y. C. Huang, I. H. Tseng, H. P. Yu, Y. K. Lin and S. L. Huang, *Thin Solid Films*, 2011, **519**, 5238–5242.
19 J. K. Malav, R. Rathod, S. Umare and D. Vidyasagar, *Mater. Res. Express*, 2018, **5**, 095309.
20 C. J. Weng, J. Y. Huang, K. Y. Huang, Y. S. Jhuo, M. H. Tsai and J. M. Yeh, *Electrochim. Acta*, 2010, **55**, 8430–8438.
21 M. Han, H. Bie, D. E. Nikles and G. W. Warren, *J. Polym. Sci., Part A:Polym. Chem.*, 2000, **38**, 2893–2899.
22 E. Huttunen-Saarivirta, V. E. Yudin, L. A. Myagkova and V. M. Svetlichnyi, *Prog. Org. Coat.*, 2011, **72**, 269–278.
23 S. Qin, C. Chen, M. Cui, A. Zhang, H. Zhao and L. Wang, *RSC Adv.*, 2017, **7**, 3003–3011.
24 S. Badaik, S. Nayak, B. Ambade and T. Kumar, *Prog. Org. Coat.*, 2025, **200**, 109046.
25 L. Dong, P. Zhang, C. Xiao, X. Tian, H. C. Du, X. Zhang and H. Zhang, *J. Alloys Compd.*, 2025, **1010**, 1–8.
26 H. Wang, L. Liu, G. Fei, Y. Duan, L. Sun and X. Hao, *Prog. Org. Coat.*, 2024, **187**, 108135.
27 K. Liu, H. Mu, M. Shu, Z. Li and Y. Gao, *Colloids Surf., A*, 2017, **529**, 356–362.
28 S. Badaik, S. Nayak, B. Ambade, and T. K. Rout, *Ceram. Int.*, DOI:DOI: 10.1016/j.ceramint.2025.12.076.
29 A. E. Eichstadt, T. C. Ward, M. D. Bagwell, I. V. Farr, D. L. Dunson and J. E. McGrath, *J. Polym. Sci., Part B:Polym. Phys.*, 2002, **40**, 1503–1512.
30 M. Dhakshnamoorthy, S. Vikram and R. Vasanthakumari, *Int. J. Sci. Eng. Res.*, 2012, **3**, 5.
31 M. G. Mohamed, A. Mahdy, R. J. Obaid, M. A. Hegazy, S. W. Kuo and K. I. Aly, *J. Polym. Res.*, 2021, **28**, 1–15.
32 B. Liang, K. Liu, J. Dai, W. Chen and W. Lu, *Polym. Degrad. Stab.*, 2024, **225**, 110807.
33 R. Purushothaman, M. Palanichamy and I. Mohammed Bilal, *J. Appl. Polym. Sci.*, 2014, **131**, 40508.
34 S. J. Varner, R. L. Vold and G. L. Hoatson, *Solid State Nucl. Magn. Reson.*, 1998, **12**, 71–85.
35 K. Nakamura, S. Ando and T. Takeichi, *Polymer*, 2001, **42**, 4045–4054.
36 X. Fang, X. Xie, C. D. Simone, M. P. Stevens and D. A. Scola, *Macromolecules*, 2000, **33**, 1671–1681.
37 T. L. Grubb, V. L. Ulery, T. J. Smith, G. L. Tullos, H. Yagci, L. J. Mathias and M. Langsam, *Polymer*, 1999, **40**, 4279–4288.
38 G. P. Wang, T. C. Chang, Y. S. Hong and Y. S. Chiu, *Polymer*, 2002, **43**, 2191–2200.
39 J. Huang and C. Kang, *J. Appl. Polym. Sci.*, 2004, **93**, 1065–1070.
40 A. Rahnamoun, D. P. Engelhart, S. Humagain, H. Koerner, E. Plis, W. J. Kennedy, R. Cooper, S. G. Greenbaum, R. Ho and A. C. T. Van Duin, *Polymer*, 2019, **176**, 135–145.
41 G. Chen, D. Li, L. Chen, Z. Lin, W. Li, B. Zhao, Z. Zhao, J. Liu, Y. Sun, J. Pang and Z. Jiang, *Chem. Eng. J.*, 2024, **500**, 156642.

42 D. Sanz, R. M. Claramunt, M. Angeles and I. Alkorta, *Tetrahedron*, 2011, **67**, 4633–4639.
43 T. P. Bender and Z. Y. Wang, *Macromolecules*, 2000, 9477–9479.
44 A. S. Mathews, I. Kim and C. Ha, *Macromol. Res.*, 2007, **15**, 114–128.
45 J. Russat, *Surf. Interface Anal.*, 1988, **11**, 414–420.
46 D. W. Zeng, K. C. Yung and C. S. Xie, *Surf. Coat. Technol.*, 2002, **153**, 210–216.
47 G. Hua, M. Cai, X. Fan and M. Zhu, *Surf. Coat. Technol.*, 2025, **511**, 132264.
48 S. S. Dong, W. Z. Yang, H. J. ye and L. Zhen, *RSC Adv.*, 2018, 28152–28160.
49 A. M. U. Ektessabi and S. Hakamata, *Thin Solid Films*, 2000, **377**, 621–625.
50 N. Khomiakova, J. Hanuš, A. Kuzminova and O. Kylián, *Coatings*, 2020, **10**, 619.
51 P. S. He, D. P. Tran, T. Y. Kuo, W. Y. Hsu, H. E. Lin, K. C. Shie and C. Chen, *Nanomaterials*, 2023, **13**, 1575.
52 J. J. Benítez, J. A. Heredia-Guerrero, S. Guzmán-Puyol, M. J. Barthel, E. Domínguez and A. Heredia, *Front. Mater.*, 2015, **2**, 59.
53 M. Liu, Y. Song, H. Qin, Z. Li, Y. Fu, C. Xiong and F. Liu, *J. Mater. Chem. C*, 2022, **45**, 17225–17235.
54 S. Liu, T. G. Chambers and W. D. Cutts, *Micron*, 2021, **145**, 103059.
55 X. Yuan, R. Yu, Y. Du and B. Lei, *Corros. Sci.*, 2024, **228**, 111810.
56 S. D. Zhang, J. Wu, W. B. Qi and J. Q. Wang, *Corros. Sci.*, 2016, **110**, 57–70.
57 T. Fu, X. Tang, Z. Cai, Y. Zuo, Y. Tang and X. Zhao, *Prog. Org. Coat.*, 2020, **139**, 105459.
58 D. I. Njoku, M. Cui, H. Xiao, B. Shang and Y. Li, *Sci. Rep.*, 2017, **7**, 1–15.
59 R. S. Scotton, L. M. Guerrini and M. P. Oliveira, *Prog. Org. Coat.*, 2021, **158**, 4–6.
60 A. Wang, K. De Silva and M. Jones.
61 C. Pawar, D. Mahajan, R. Bind, D. Jadhao, P. Desai, H. Bagde and A. More, *Arabian J. Sci. Eng.*, 2023, **48**, 7841–7854.
62 J. Chavhan, R. Rathod, S. Umare, J. Desai, S. Sapate and Y. Mahajan, *Prog. Org. Coat.*, 2023, **178**, 107496.
63 S. Nayak, S. Badaik, T. Kumar and S. Patra, *Mater. Chem. Phys.*, 2026, **348**, 131564.
64 R. Chantarachindawong, T. Osotchan and P. Chindaudom, *J. Sol-Gel Sci. Technol.*, 2016, **79**, 190–200.
65 J. Zheng, Z. M. Png, S. H. Ng, G. X. Tham, E. Ye, S. S. Goh, X. J. Loh and Z. Li, *Mater. Today*, 2021, **51**, 586–625.
66 I. M. Kalogeras, Glass-Transition Phenomena in Polymer Blends, 2016.
67 M. Kotera, B. Samyul, K. Araie, Y. Sugioka, T. Nishino, S. Maji, M. Noda, K. Senoo, T. Koganezawa and I. Hirosawa, *Polymer*, 2013, **54**, 2435–2439.
68 M. H. Tsai, P. C. Chiang, W. T. Whang, C. J. Ko and S. L. Huang, *Surf. Coat. Technol.*, 2006, **200**, 3297–3302.
69 Y. Yang, W. Chen, Z. Li, G. Huang and G. Wu, *Chem. Eng. J.*, 2022, **450**, 138424.
70 M. Wu, G. Cao and Z. Xiao, *Adv. Compos. Hybrid Mater.*, 2025, **8**, 1–6.
71 K. I. Aly, M. Gamal, O. Younis and M. H. Mahross, *Prog. Org. Coat.*, 2020, **138**, 105385.
72 A. Mahdy, K. I. Aly and M. Gamal, *Heliyon*, 2023, **9**, e17977.